



A novel green synthesis approach for improved photocatalytic activity and antibacterial properties of zinc sulfide nanoparticles using plant extract of *Acalypha indica* and *Tridax procumbens*

S. Kannan¹ · N. P. Subiramaniam¹ · M. Sathishkumar¹

Received: 9 February 2020 / Accepted: 1 May 2020 / Published online: 9 May 2020
© Springer Science+Business Media, LLC, part of Springer Nature 2020

Abstract

In this present work, improved photocatalytic activity and antibacterial properties of zinc sulfide (ZnS) nanoparticles using plant extract of *Acalypha indica* (A:ZnS) and *Tridax procumbens* (T:ZnS) via novel green synthesis route had been reported. X-ray diffraction (XRD), transmission electron microscopy (TEM), and Energy dispersive X-ray spectroscopy (EDX) were used to investigate the crystal structure, surface morphology, and elemental composition analysis, respectively. The optical properties and functional group analysis of the samples were done using UV–visible, photoluminescence, and Fourier transform infrared spectroscopy (FTIR). The influence of *Acalypha indica* (A:ZnS) and *Tridax procumbens* (T:ZnS) plant extract concentration on the structural, surface morphology, optical, antibacterial, and photocatalytic activity has been systematically investigated. XRD results are suggested that ZnS hexagonal wurtzite crystal structure formed during biosynthesis process. TEM and SAED images show the hexagonal- and spherical-shaped structure in morphology with average diameter around 5–20 nm which is good agreement with the grain size calculated from XRD. Optical properties were found to have considerable red shift in the absorption edge and decreasing band gap was observed for A:ZnS/T:ZnS (2.96 eV) when compared to pure ZnS (3.36 eV). The antibacterial properties of ZnS/A:ZnS/T:ZnS nanoparticles were investigated using in vitro disk diffusion method against human pathogenic microorganisms. The inhibition zone of biosynthesized ZnS nanoparticles increased by increasing plant extracts concentration. This result conformed that A:ZnS/T:ZnS nanoparticles have more potential as antibiotic when compared with pure ZnS. Besides, Biosynthesized T:ZnS (40 ml) nanoparticles showed high surface area (131.84 m²/g) and larger pore size (12.15 nm) than pure ZnS sample; this high surface area may offer more active sites to enhance photocatalytic ability. The dye degradation properties of methylene blue dye (MBD) were investigated using the ZnS/A:ZnS/T:ZnS nanoparticles under visible light irradiation. The results show that T:ZnS (40 ml) has excellent photocatalytic performance towards MBD such as high degradation efficiency (98%) and more cyclic stability than other ZnS samples. The role of plant extract on dye degradation properties was discussed based on the possible inhibition of photogenerated electron–hole pair recombination during dye degradation under visible light irradiation.

1 Introduction

The removal of organic pollutants in waste water using semiconductor nanomaterials has attracted a lot of attention as an important environmental protection procedure. Wide and direct band gap semiconductors are of great interest in photocatalysis with ZnS representing an important role [1]. In recent years, biosynthesis of nanoparticles

for removal of organic pollutants in waste water has gained much attention to develop clean and renewable materials. Among II–VI group semiconductors, ZnS is a promising semiconductor used for advanced electronics and optoelectronics devices owing to its interesting physical, chemical, optical, and electrical properties [2, 3]. Many attempts have been made to study and compare the photocatalytic activity of different semiconductors and ZnS was found to be one of the most effective catalysts. Nanostructure of ZnS has attracted more interest because of its considerable photocatalytic efficiency and good stability and several works have reported the high photocatalytic efficiency of ZnS nanoparticles [4, 5]. ZnS is a promising catalysis semiconductor material with wide band gap of 3.63 eV and

✉ S. Kannan
nasckannan.s@nehrucolleges.com

¹ Department of Electronics, Nehru Arts and Science College, Coimbatore, Tamilnadu, India

40 meV binding energy. Owing to these potential optical properties, ZnS has unique catalytic characteristics which result in rapid generation of electron–hole pairs by photo-excitation and negative reduction of excited electrons [6]. ZnS has an excellent photoresponsivity and acts as photocatalyst to excite electrons from VB (valance band) to CB (conduction band) and to generate electron–hole pairs which can initiate redox reaction and migration with oxygen and water and then degrade organic molecules or reduce ions absorbed on the surface of ZnS owing to their large shape and surface-to-volume ratio [7]. Methylene Blue (MB) (CI 52,015) is a heterocyclic aromatic chemical compound with the molecular formula $C_{16}H_{18}N_3SCl$. It has many uses in a range of different fields, such as biology and chemistry. At room temperature, it appears as a solid, odorless, dark green powder, which yields a blue solution when dissolved in water. The hydrated form has 3 molecules of water per molecule of MB [8]. MB is widely used as a redox indicator in analytical chemistry. Solutions of this substance are blue when in an oxidizing environment, but will turn colorless if exposed to a reducing agent. The redox properties can be seen in a classical demonstration of chemical kinetics in general chemistry, the "blue bottle" experiment. Typically, a solution is made of glucose (dextrose), MB, and sodium hydroxide. Upon shaking the bottle, oxygen oxidizes methylene blue, and the solution turns blue [9]. In this work, a model textile reactive dye methelene blue is taken for the photocatalytic degradation using prepared ZnS/A:ZnS/T:ZnS nanoparticles under visible light irradiation. However, many studies have reported the photocatalytic properties of semiconductor catalysts such as SnO_2 [10], $Cr:WO_3$ [11], $Cu:SnO_2$ [12] which absorb visible lights and capture the photo-induced electrons into the CB which can generate the formation of reactive radicals, hydroxyl radicals, and superoxide radical ions; these radicals are more crucial for the degradation of the MB dye solution. At the same time, doping or stabilizing materials play an important role to create a donor level below the CB of source material to increase absorption intensity of visible light. This intermediate energy level between the CB and VB may be attributed to high surface area of semiconductor catalyst leading to the formation of radical anions which produce reactive oxygen species (ROS) in dye degradation oxidation process under visible light illumination. Hence, in the present work, we have synthesized ZnS nanoparticles using different plant extract concentrations (20 ml and 40 ml) of *Acalypha indica* and *Tridax procumbens* and investigated their structural, optical, and antibacterial and dye degradation properties under visible light irradiation. To the best of our knowledge, this is the first preliminary report about the MB dye degradation properties of biosynthesized ZnS nanoparticles using

Acalypha indica and *Tridax procumbens* plant extract with different optimum concentration.

2 Experimental procedure

2.1 Preparation of plant extracts

Entire fresh plants of *Acalypha indica* and *Tridax procumbens* were collected from Vellingiri Hills, Coimbatore, Tamilnadu and it was authenticated by Botanical Survey of India, Coimbatore. Collected plants were washed in running tap water followed by deionized water to remove dust and soil and shadow dried for 10 days at room temperature. Dried plant material were powdered by the using mixer and 200 g of plant powder was subjected to extraction in 200 ml of methanol solvent by using Soxhelt apparatus [13] and prepared plant extracts were used for ZnS fabrication.

2.2 Synthesis of ZnS/A:ZnS/T:ZnS nanoparticles

The ZnS/A:ZnS/T:ZnS nanoparticles were prepared using plant extracts. In typical synthesis process of pure ZnS, 100 ml of each homogeneous solution of 1 M (16.14 g) (Zinc sulfate— $ZnSO_4 \cdot 7H_2O$) and 1 M (7.61 g) of ($NH_2CS NH_2$ —Thiourea) were prepared separately. Then, 1 molar ratio of thiourea solution was added drop by drop into 1 molar ratio of Zinc sulfate. While adding thiourea solution, white precipitate appeared and the mixture solution was stirred for 60 min at room temperature using a magnetic stirrer. A nanocolloid solution was formed which was centrifuged at 2000 rpm for 20 min. The precipitate was then dried at 100 °C for 5 h using air furnace. The dried precipitate was allowed to cool down naturally at room temperature and ground into powder using a mortar and pestle to obtain ZnS nanoparticles. For biosynthesis of ZnS nanoparticles, the same procedure was followed, but two different concentration of methanol plant extracts (20 ml and 40 ml) were added to the final solution after adding $NH_2CS NH_2$ solution. The pH value of the final solution was found to be 7.7 and it was maintained for all the prepared samples. For better comparative evaluation, *Acalypha indica* plant extract-synthesized ZnS is designated as A:ZnS and *Tridax procumbens* plant extract-synthesized ZnS is designated as T:ZnS.

2.3 Characterization

The crystal structure of the prepared ZnS nanoparticles were characterized by X'per PRO model with $CuK\alpha$ radiation ($\lambda = 1.54056 \text{ \AA}$) in the 2θ range from 20° to 80° with 0.1° step size. Morphology of the ZnS nanoparticles were studied by using Transmission Electron Microscopy and Selected Area Electron Diffraction by Tecnai

G20 20 XTWIN with operating voltage range from 40 to 200 kV with high magnification capacity and high resolution mode. Chemical composition analysis was studied by SEM attached with energy dispersive analysis X-ray spectra CARL-ZESIS EVOMA 15. Optical absorbance properties of the prepared samples were recorded by Perkin Elmer UV/VI/NR spectrometer with wavelength range from 300 to 900 nm at room temperature and Photoluminescence spectra of the samples were recorded by Perkin Elmer LS 55 spectrometer with 40 w Xenon lamp. Different bimolecular bonding functional groups were analyzed by JASCO FT/IR-6600 with spectral range from 400 to 4000 cm^{-1} .

2.4 Antibacterial susceptibility test preparation

Human pathogenic microorganisms were obtained from Microbial Type Culture Collection (MTCC) Institute of Microbial Technology, Chandigarh, India. Antibacterial activity of prepared ZnS nanoparticles was determined by In vitro disk diffusion method against *S.aures* and *P.aeruginosa*. Microorganisms were maintained 4 °C on the slopes nutrient ager, and MHA plates were incubated for 24 h at 37 °C. 15 ml of molten sterile MHA media was poured onto the petriplates and allowed to solidify for 5 min. 0.1% of the stock culture was swabbed on the MHA plates and 6 mm of sterile disks which have 60 μl concentration of plant extract were placed on the MHA plate surface and amoxicillin used as positive control. The prepared ZnS nanoparticles were loaded on the sterile disk surface and the loaded MHA plates were incubated at 37 °C overnight, and the inhibition zone formed around the disk was calculated by a transparent millimeter ruler [14].

2.5 Dye degradation experiment setup

Dye degradation activity was carried out in a specially designed reactor under 500 W halogen lamp irradiation which was used as visible light source. Distance between the lamp and liquid surface (methylene blue dye) was kept at 5 cm. 1.0 mg of pure and biosynthesized ZnS was added as catalyst to 100 ml of methylene blue dye (1×10^{-5} M) aqueous solution and stirred in dark for 30 min to attain equilibrium condition. For comparative evaluation, ZnS catalyst-added dye solution was kept under visible light irradiation for 180 min. At regular interval of 30 min, 3 ml of the dye sample was taken from mixture, mixed well, and the dye degradation absorption spectra was recorded using Perkin Elmer UV/VI/NR spectrometer and centered wavelength of methylene blue dye was found to be 631 nm. The dye degradation efficiency was calculated by the expression [15, 29]

$$\text{Degradation efficiency} = \frac{A_0 - A_t}{A_t} \times 100\%$$

where A_t is absorbance at t minutes and A_0 is absorbance at $t=0$

3 Results and discussion

3.1 Structural analysis

Figure 1 shows XRD pattern and of ZnS/A:ZnS/T:ZnS nanoparticles prepared using different concentrations of plant extract. From this XRD pattern, all the ZnS/A:ZnS/T:ZnS nanoparticles exhibit sharp and high intense peaks which indicate that nanoparticles are highly crystalline. The diffraction pattern of ZnS/A:ZnS/T:ZnS nanoparticles exhibit broad diffraction peak at 2θ position of 28.57° corresponding to (016) plane reflections. This diffraction result shows that there is no other impurity detected. This peak has been well matched with the JCPDS card no. 83-2336, which confirms the formation of ZnS hexagonal wurtzite crystal structure. Moreover, strong diffraction peak (016) was observed for A:ZnS/T:ZnS nanoparticles and peak intensity increased with increasing plant extract concentration (see Fig. 1b–e).

Figure 1b and c shows XRD diffraction pattern of A:ZnS nanoparticles synthesized by using 20 ml and 40 ml concentration of plant extract. This diffraction result shows that some new diffraction peaks appear at 2θ position of 23.72° , 28.57° , 47.52° , and 62.78° corresponding to (001), (016), (012), and (021) plane reflections, respectively. It indicates that the ZnS exhibits hexagonal wurtzite structure. From the XRD results, it can be seen that the intensity of the diffraction peaks increases with the increasing plant extract

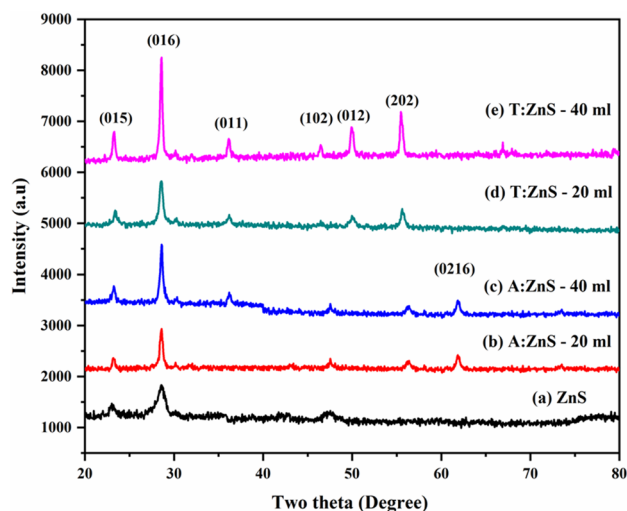


Fig. 1 [A] XRD pattern of ZnS/A:ZnS/T:ZnS nanoparticles

concentration, which means the crystallinity of the nanoparticles gets increased as the plant extract solution gets increased. No characteristic peaks corresponding to impurities are detected which clearly suggests the formation of pure ZnS. It proves that crystalline growth of the ZnS is enhanced due to the presence of secondary metabolites like flavonoids, phenols, saponins, alkaloids, steroids [13, 15].

Figure 1d and e shows XRD pattern of T:ZnS nanoparticles synthesized by 20 ml and 40 ml concentration of plant extract. This XRD result shows that the high-intensity diffraction peaks appeared at 2θ position of 23.72° , 28.57° , 50.37° , and 55.56° corresponding to (001), (016), (012), and (202) plane reflections, respectively. The data are in good agreement with the hexagonal wurtzite structure of ZnS. It can be seen from the diffraction pattern, as the concentration of the plant extract increases, the intensity of the diffraction peak also increases which indicates that the bioactive compounds in the plant extract play a major role to synthesis of a shape- and size-controlled nanoparticles [16]. Besides, from the biosynthesized ZnS XRD pattern, small peak shift towards higher position was found and this shift was associated with the biomolecules presence in the plant extract substitution and/or interstitial in the ZnS crystal lattice of A:ZnS/T:ZnS samples and the higher and lower shifts observed in the peak position were dependent on ionic radius effect of changes in plant extract concentration [35]. Further, the non-linear three exponential filter curves are shown in Fig. 2a. it was noticed that the major peak (016) plane intensity was gradually increased when increasing plant extract concentration and it is shows that T:ZnS-40 ml sample intensity was found to be two times higher than pure ZnS peak intensity and these results suggest that biosynthesized ZnS was highly crystalline in nature. The lattice parameter of the prepared ZnS/A:ZnS/T:ZnS nanoparticles hexagonal structure were estimated by following equation

$$\frac{1}{d_{hkl}^2} = \frac{4}{3} \frac{h^2 + hk + k^2}{a^2} + \frac{l^2}{c^2} \quad (1)$$

The lattice constant was calculated as $a = b = 3.823 \text{ \AA}$ and $c = 56.6 \text{ \AA}$ for all the diffraction peaks corresponding to the reflection planes. The average crystalline size was calculated using Debye–Scherrer Eq. (2) [17].

$$D_{hkl} = \frac{K\lambda}{\beta_{hkl} \cdot \cos\theta_{hkl}} \quad (2)$$

where D_{hkl} is the crystalline particle size perpendicular to the plane (hkl), K is constant, and λ is X-ray wavelength, θ_{hkl} is the Braggs angle of the diffraction peak. Full width at half maximum of the diffraction peak is β_{hkl} . Moreover, the unit cell volume of the ZnS/A:ZnS/T:ZnS nanoparticles was estimated by the $V = a^3$ relationship and is listed in Table 1.

It shows that changes in unit cell parameter of the nanoparticles of ZnS are different from bulk ZnS and at the same time, plant extract-mediated samples verify successful incorporation of crystal growth of ZnS lattice. The dislocation density (δ) and lattice microstrain (ϵ) were calculated by using following Williamson Smallman relations, respectively [18]:

$$\delta = \frac{1}{D^2} \quad (3)$$

$$\epsilon = \frac{a - a_0}{a_0} \times 100 \quad (4)$$

Based on these relations, increase in crystalline size and crystalline quality decreases dislocation density that represents the amount of defect in the samples which is defined as the length of dislocation line per unit volume of the crystal. Table 1 shows that plant extract-capped samples resulted in an increase in dislocation density of ZnS. Besides, the calculated lattice parameter and micro strains value decreased by increasing the plant extract concentration when compared with pure ZnS, this is due to mismatch in the radius of zinc ions. From this XRD pattern, the synthesized ZnS/A:ZnS/T:ZnS nanoparticles crystallite size increases with increase in plant extract concentration. The calculated crystallite size of the (016) plane was found to be 9 nm and further it was increased to 23 nm for A:ZnS-40 ml and 30 nm for T:ZnS-40 ml. From these results, it is evident that the plant extracts influence to increase the structural properties of ZnS nanoparticles.

3.2 Morphological and elemental composition analysis

The surface morphology and elemental composition analysis of synthesized ZnS/A:ZnS/T:ZnS nanoparticles using plant extract were studied by Transmission electron microscopy (TEM) and energy dispersive X-ray (EDX). Figure 2b–f represent the TEM and selected area electron diffraction (SAED) images of ZnS/A:ZnS/T:ZnS nanoparticles. Pure ZnS nanoparticles are small and have almost hexagonal-like structure, A:ZnS/T:ZnS nanoparticles have spherical-like structure in morphology, particle size of pure ZnS was found to be 5 nm, and A:ZnS/T:ZnS nanoparticles was found to be 10 nm for A:ZnS and 20 nm for T:ZnS and this estimated grain size values are in good agreement with those obtained from the XRD pattern. The SAED pattern of ZnS/A:ZnS/T:ZnS nanoparticles showed concentric rings which indicate nanoparticle nature of materials. These fringes are well matched with the (016) plane reflection of hexagonal ZnS phase; at the same time, some of the polycrystalline rings are observed for A:ZnS/T:ZnS nanoparticles which could imply some crystallinity and large grain of the samples.

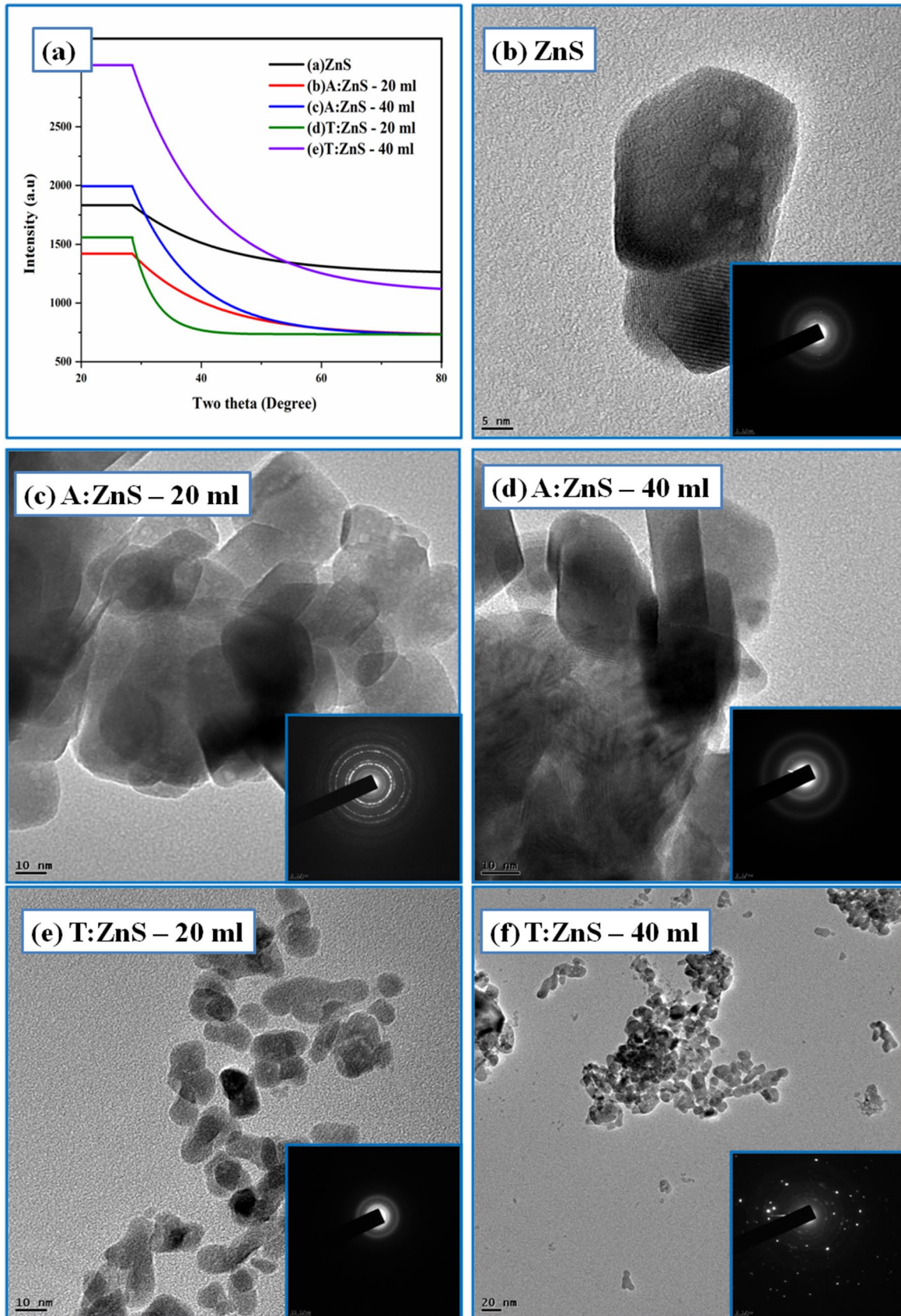


Fig. 2 a Non-linear exponential filter curve. b ZnS, c A:ZnS-20 ml, d A:ZnS-40 ml, e T:ZnS-20 ml, and f T:ZnS-40 ml nanoparticles TEM and SAED images

Table 1 Calculated structural parameters of ZnS/A:ZnS/T:ZnS nanoparticles

ZnS nanoparticles	2θ (<i>hkl</i>)	D spacing	FWHM (Radian)	Lattice constants		Average crystallite size (nm)	Dislocation density (δ) 10^{14} lin/m ²	Microstrain (ϵ) ($10^4/\text{lin}^2/\text{m}^4$)
				Lattice a (\AA)	Parameter c (\AA)			
ZnS	28.57 (016)	3.121	0.944	3.823	56.6	9	0.000353	0.004091
A:ZnS-20 ml	28.57 (016)		0.393			22	0.000062	0.001720
A:ZnS-40 ml	28.57 (016)		0.379			23	0.000057	0.001650
T:ZnS-20 ml	28.57 (016)		0.449			19	0.000081	0.001965
T:ZnS-40 ml	28.57 (016)		0.290			30	0.000034	0.001269

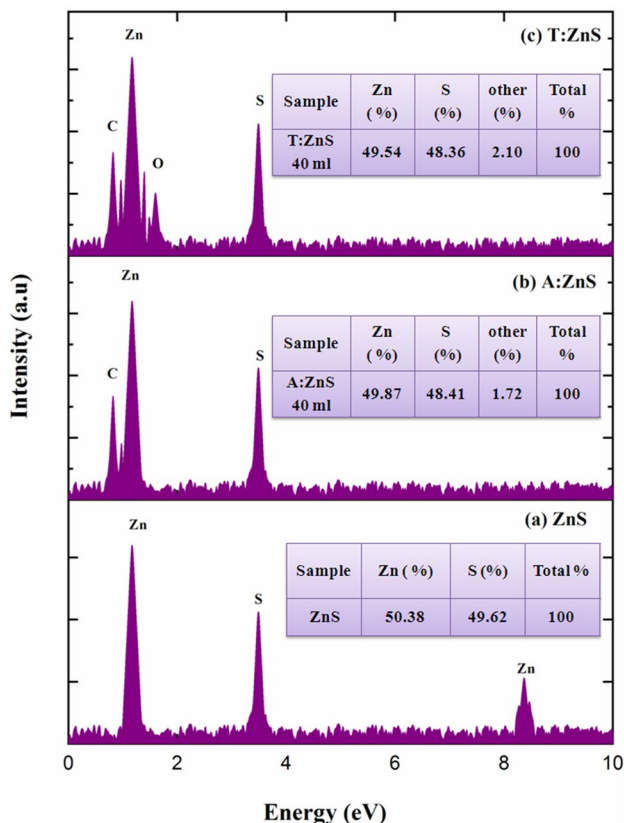


Fig. 3 EDAX spectra of ZnS/A:ZnS/T:ZnS nanoparticles

Figure 3a–c show the EDX analysis of prepared ZnS/A:ZnS/T:ZnS nanoparticles; the resulting Fig. 3a shows pure ZnS EDX spectrum which contained only zinc and sulfur composition thus confirming the high purity of ZnS without presence of any other impurities. Figure 3b–c show A:ZnS/T:ZnS nanoparticles containing zinc and sulfur composition with some organic impurities presence i.e., carbon and oxygen; at the same time, its confirmed sulfur ratio was gradually decreased by increasing plant extract concentration, which confirms that the biomolecules of plant extract were substituted in ZnS host lattice and Table 2 shows the different atomic ratio of synthesized ZnS/A:ZnS/T:ZnS nanoparticles.

3.3 Optical properties

The optical properties of ZnS/A:ZnS/T:ZnS nanoparticles were analyzed by UV absorbance and transmittance spectra as shown in Figs. 4 and 5. The absorbance spectra of prepared ZnS were investigated in the wavelength range from 300 to 800 nm as shown in Fig. 3. Strong absorbance peaks were found in the range of 300–450 nm. The strength of the absorbance peaks of ZnS, A:ZnS-20 ml, A:ZnS-40 ml, T:ZnS-20 ml, and T:ZnS-40 ml nanoparticles were found to be 339 nm, 391 nm, 408 nm, 414 nm, and 422 nm, respectively. From this investigation, the absorption peaks were red shifted towards higher wavelength by increasing plant extract concentration due to electron excitation from valance band to conduction band [19]. Optical transmittance of prepared ZnS nanoparticles were measured in the wavelength range of 300–1000 nm

Table 2 EDX analysis of ZnS/A:ZnS/T:ZnS nanoparticles

ZnS nanoparticles	Zn content %	S content %	Other content %	Total %	Band gab energy (eV)
ZnS	50.38	49.62	-	100	3.36
A:ZnS-20 ml	50.12	48.65	1.23	100	3.25
A:ZnS-40 ml	49.87	48.41	1.72	100	3.16
T:ZnS-20 ml	50.18	48.74	1.08	100	3.09
T:ZnS-40 ml	49.54	48.36	2.10	100	2.97

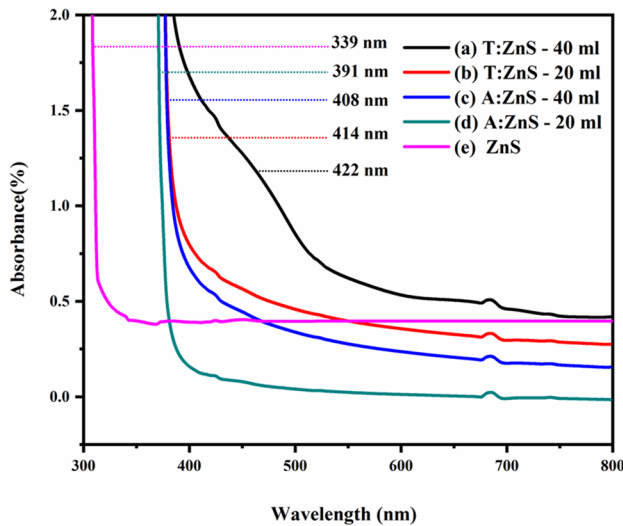


Fig. 4 Optical absorbance of ZnS/A:ZnS/T:ZnS nanoparticles

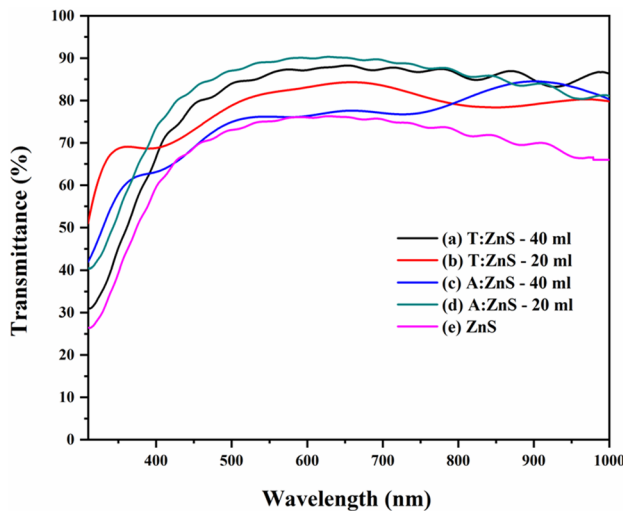


Fig. 5 Optical Transmissions of ZnS/A:ZnS/T:ZnS nanoparticles

as shown in Fig. 4. Optical transmittance of ZnS, A:ZnS-20 ml, A:ZnS-40 ml, T:ZnS-20 ml, and T:ZnS-40 ml nanoparticles were 68%, 83%, 80%, 82%, and 85%, respectively, in the visible range.

This transmittance was slightly increased for A:ZnS-20 ml and A:ZnS-40 ml which showed that increase in plant extract concentration increases the transmittance. This due to free electron and holes absorption effect of ZnS [20]. The transmittance of ZnS/A:ZnS/T:ZnS nanoparticles increased around 18% with increase in the plant extract concentration. The optical band gap energy of the prepared nanoparticles was determined by absorbance (A) at different wavelength (λ) with absorption coefficient (α); Beer–Lamberts relation (Eq. 5) was used to calculate the absorption coefficient (α).

$$\alpha = \frac{2303A}{d} \quad (5)$$

$$ah\nu = K(h\nu - E_g)^n \quad (6)$$

where K is the constant, $h\nu$ is incident photon energy E_g is band gap energy and n depends on the type of transition associated with indirect and direct electron band which equal to value of $1/2$, 2 , $3/2$, and 3 , respectively. The direct band gap value was determined by plotting a graph between $h\nu$ versus $(ah\nu)^2$ (see Fig. 6). Calculated band gap energy of ZnS, A:ZnS-20 ml, A:ZnS-40 ml, T:ZnS-20 ml, and T:ZnS-40 ml nanoparticles were found to be 3.36 eV, 3.25 eV, 3.16 eV, 3.09 eV, and 2.97 eV, respectively. From this result T:ZnS-40 ml exhibit low band gap energy when compared with pure ZnS due to higher wavelength absorption. Moreover, pure ZnS band gap value increases with increasing plant extract concentration; this may be possibly due to change in phase morphology and increasing particle size and red shift of the band gap which probably occur due to the growth of grains and decrease in defect states of nearest band edge of (NBE) wavelength in visible region [21]. Based on the reduction in the band gap energy, the T:ZnS-40 ml catalyst is more appropriate in the efficiency of photocatalyst than other catalysts.

Photoluminescence spectroscopy is very vital to implement and explore the surface defects, impurities, energy bands of the samples. In addition, it can be a useful method to determine recombination process of the electron–hole pairs. The photoluminescence spectrum of obtained ZnS/A:ZnS/T:ZnS nanoparticles were recorded at room temperature in the wavelength range of 300–700 nm with excitation wavelength of 338 nm. Figure 7 shows the photoluminescence spectrum which contains four emission peaks centered at 415 nm, 421 nm, 495 nm, and 576 nm, respectively. From this result, photoluminescence spectrum of pure ZnS

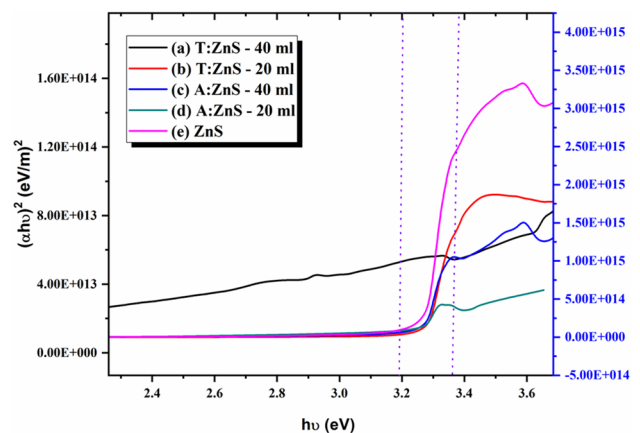


Fig. 6 Tauc plots for ZnS/A:ZnS/T:ZnS nanoparticles

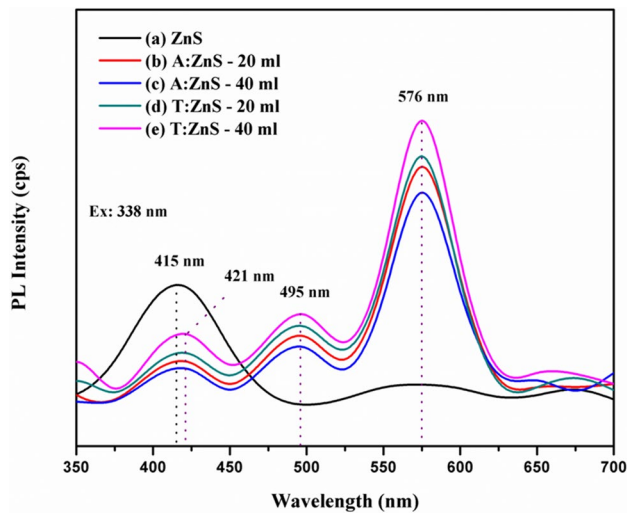


Fig. 7 PL spectra of ZnS/A:ZnS/T:ZnS nanoparticles

nanoparticles shows weak intensity compared with plant extract-capped ZnS. From this, we can conclude that plant extract influences the surface properties of the ZnS crystals. The high-intensity emission peak seen at 415 nm was due to intrinsic emission of (pure ZnS) crystals. Interestingly, there were no broad peaks in green emission region which may be attributed to the defect in ZnS crystal due to reunion of sulfur sources [22]. Broad and strong green emission peaks for A:ZnS/T:ZnS nanoparticles show dominant green emission peak located at 576 nm which was corresponding to recombination of electron from sulfur vacancies energy level with holes from zinc vacancies. High emission peak was located for T:ZnS nanoparticles which may be due to the surrounding ligand field which strongly influenced energy level splitting of plant extract in the ZnS host lattice [23]. However, in the case of A:ZnS/T:ZnS nanoparticles, high surface-to-volume ratio was found which grades in the development of the crystal growth.

3.4 FTIR analysis

Figure 8 shows Fourier transform infrared spectrum (FTIR) of ZnS/A:ZnS/T:ZnS nanoparticles. Prepared ZnS/A:ZnS/T:ZnS nanoparticles showed several peaks at 499, 615, 895, 1140, 1475, 1510, 2243, and 3035 cm^{-1} . The peaks appeared at 499 cm^{-1} and 615 cm^{-1} due to stretching vibration of zinc and sulfur bond and with increasing *Acalypha indica* plant extract concentration the intensity of the peak also increased which confirmed high growth of zinc crystal; at the same time, when increasing *Tridax procumbens* plant extract, sulfur bond was increased which matched with XRD and TEM investigation. The sharp and broad peaks at 895 and 1140 cm^{-1} observed were due to the stretching of (C–C) and (C–O) bond owing to alkenes, epoxy, and amino

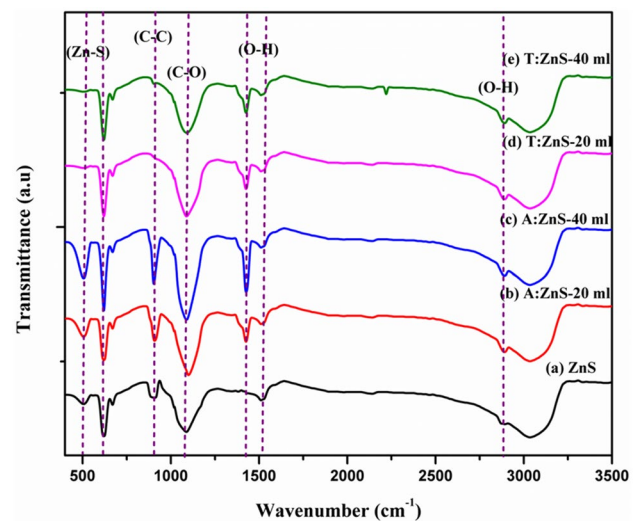


Fig. 8 FTIR spectra of ZnS/A:ZnS/T:ZnS nanoparticles

acids [24, 25]. It was observed that with increasing *Acalypha indica* plant extract concentration, the intensity of the peak was increased; at the same time, when increasing *Tridax procumbens* plant extract concentration, intensity of the peak was decreased. From pure ZnS result, the peak at 1510 cm^{-1} corresponded to (O–H) bending vibration, and this peak was shifted towards lower wavelength of 1475 cm^{-1} for A:ZnS/T:ZnS nanoparticles due to the presence of hydroxyl group [26]. The bending vibration of CO_2 stretching and broad (O–H) bonding were observed at 2243 cm^{-1} and 3035 cm^{-1} which were ascribed to superposition of the hydroxyl group and the stretching vibration of the adsorbed water molecule in the ZnS/A:ZnS/T:ZnS nanoparticles, respectively [27].

3.5 Antibacterial activity

The antibacterial activity of ZnS/A:ZnS/T:ZnS nanoparticles was investigated by In vitro disk diffusion method against *Staphylococcus aureus* (*S. aureus*) and *Pseudomonas aeruginosa* (*P. aeruginosa*) microorganisms. Figure 9 and Table 3 show diameter of inhibition zone against both Gram-positive (*S. aureus*) and Gram-negative (*P. aeruginosa*) microorganisms. The maximum inhibition zone of ZnS, A:ZnS-20 ml, A:ZnS-40 ml, T:ZnS-20 ml, and T:ZnS-40 ml nanoparticles were observed to 16 mm, 17 mm, 17 mm, 19 mm, and 20 mm against *P. aeruginosa* (16 mm) at concentration of 60 mg/ml, respectively. Minimum zone of ZnS, A:ZnS-20 ml, A:ZnS-40 ml, T:ZnS-20 ml, and T:ZnS-40 ml nanoparticles were observed at 14 mm, 15 mm, 16 mm, 18 mm, and 19 mm against *S. aureus* at concentration of 60 mg/ml, respectively. From this investigation, it is clearly seen that, the concentration of the plant extract increased once diameter of inhibition zone also increased; at the same

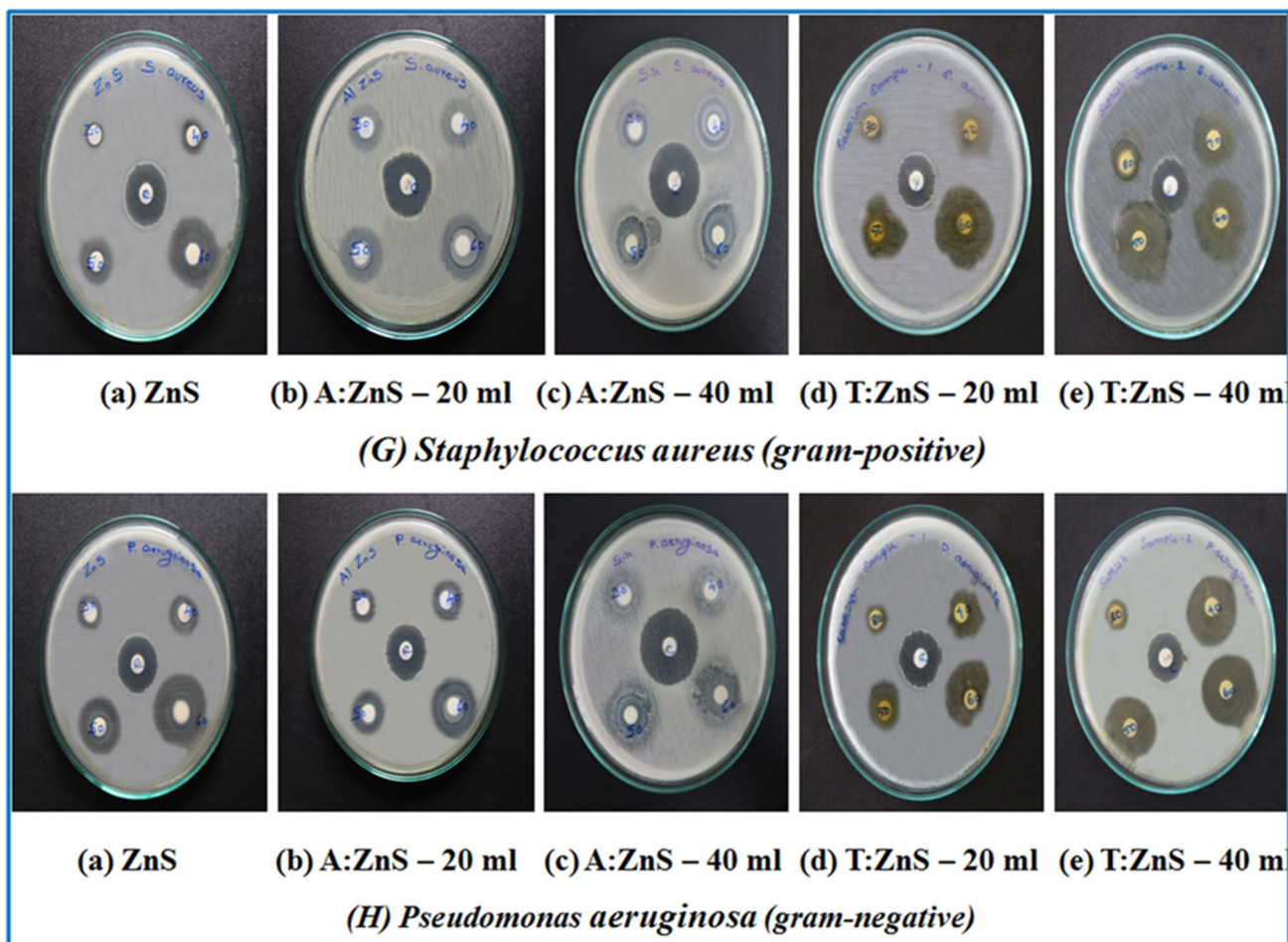


Fig. 9 Zone of Inhibitions against (G) *Staphylococcus aureus* (H) and *Pseudomonas aeruginosa* microorganisms of ZnS/A:ZnS/T:ZnS nanoparticles

Table 3 The diameter of inhibition zone of ZnS/A:ZnS/T:ZnS nanoparticles

ZnS concentrations (µg/ml)	<i>S. aureus</i> (Gram positive) inhibition zone in mm				<i>P. aeruginosa</i> (Gram negative) inhibition zone in mm			
	30	40	50	60	30	40	50	60
ZnS	01	03	07	14	02	05	10	16
A:ZnS-20 ml	03	05	08	15	02	06	11	17
A:ZnS-40 ml	03	06	11	16	04	07	13	17
T:ZnS-20 ml	03	06	18	18	04	08	12	19
T:ZnS-40 ml	04	08	15	19	04	10	15	20

time, increase in concentration of antibiotic increased inhibition zone in the control plates. From the comparison, we conclude that excellent inhibition zone was observed for T:ZnS-40 ml nanoparticles against Gram-negative bacteria than Gram-positive bacteria which may be due to the cell structure of bacteria. Here, A:ZnS/T:ZnS nanoparticles have excellent antibacterial activity than pure ZnS due to the presence of secondary metabolites such as flavonoids, phenols, saponins, alkaloids, and steroids in the plant extract;

these react with amide phosphate and carboxyl groups in the protein of cell membrane which disrupts the bacterial cell wall [28, 29]. Mailander et al. reported an effective rate of photoinactivation the microorganisms must have for surface interactions with the photocatalyst. The reactive oxygen species (ROS) generated during photocatalysis will first damage the cell wall of the microorganisms present in the pollutants and the ROS first breaks down the lipopolysaccharide layer of the cell wall; this then leads to the attack of the

peptidoglycan layer, peroxidation of the lipid membrane, and oxidation on the proteins membrane [30].

3.6 BET surface analysis

A standard approach for the specific surface area measurement is the Brunauer Emmett Teller (BET). The large surface area and smaller particle size are the main parameters in photodegradation. Figure 10a and b show the N_2 absorption–desorption tests and pore size distribution of pure and biosynthesized ZnS nanoparticles. It depicts that prepared samples showed H1 hysteresis loop isotherms of type IV which indicate that prepared samples are of mesoporous nature [31]. The BET specific surface area of prepared samples was found to be 38 m^2/g , 58 m^2/g , 91 m^2/g , 121 m^2/g , and 131.84 m^2/g for ZnS, A:ZnS-20 ml, A:ZnS-40 ml, T:ZnS-20 ml and T:ZnS-40 ml samples, respectively. The prepared samples pore size distribution was determined using Barrett Joyner Halenda approach from the desorption branch of isotherm and pore diameter was found to be 12.15 nm, 18.15 nm, 20.79 nm, 24.03 nm, and 29.74 nm for ZnS, A:ZnS-20 ml, A:ZnS-40 ml, T:ZnS-20 ml, and T:ZnS-40 ml samples, respectively. This BET analysis concluded that T:ZnS-40 ml nanocomposites with large surface area could effectively increase transportation of electron and ions at the interface to improve dye degradation performance [32].

3.7 Methylene blue dye degradation properties

The methylene blue dye degradation properties of ZnS/A:ZnS/T:ZnS nanoparticles were evaluated under visible light. Without adding catalyst, methylene blue dye

degradation process was observed under visible light to check the concentration efficiency. From this result, methylene blue dye got degraded by only 2% after 180 min irradiation under visible light. On the other side, the same experimental degradation process was repeated with 1.0 mg of ZnS/A:ZnS/T:ZnS nanoparticles as photocatalyst. During the irradiation, diffusion of charge carrier to the surface of the particle was observed which interact with water molecules to produce high reactive species of (O_2^-) peroxide and (OH^\cdot) hydroxyl radical that are responsible for dye degradation. This degradation performance is dependent on the high surface area of the crystal and morphology which might enhance the properties of photo-generated electron–hole pairs. ZnS as a catalyst was involved in adsorption of the dye onto surface of ZnS nanoparticles when irradiated with visible light. This exposure led to the generation of electron hole pairs in ZnS. These photo-generated electrons in the conduction band of ZnS interacted with oxygen molecules forming superoxide anions radicals which were adsorbed on the surface of ZnS. The holes generated in the valance band of ZnS react with surface hydroxyl groups to produce highly reactive hydroxyl radicals. These highly reactive hydroxyl radicals and superoxide radicals can react with methylene blue dye adsorbed on ZnS leading to its degradation [33].

Figure 11 shows the time-dependent visible light absorption spectra of methylene blue dye using ZnS/A:ZnS/T:ZnS nanoparticles catalyst as a function of wavelength from 400 to 800 nm during various time intervals (0 to 180 min). The rate of degradation was recorded with respect to the change in the absorbance intensity peak; the prominent peak at 631 nm decreases gradually with increase in irradiation time which indicates that methylene blue dye had been degraded. The degradation efficiency

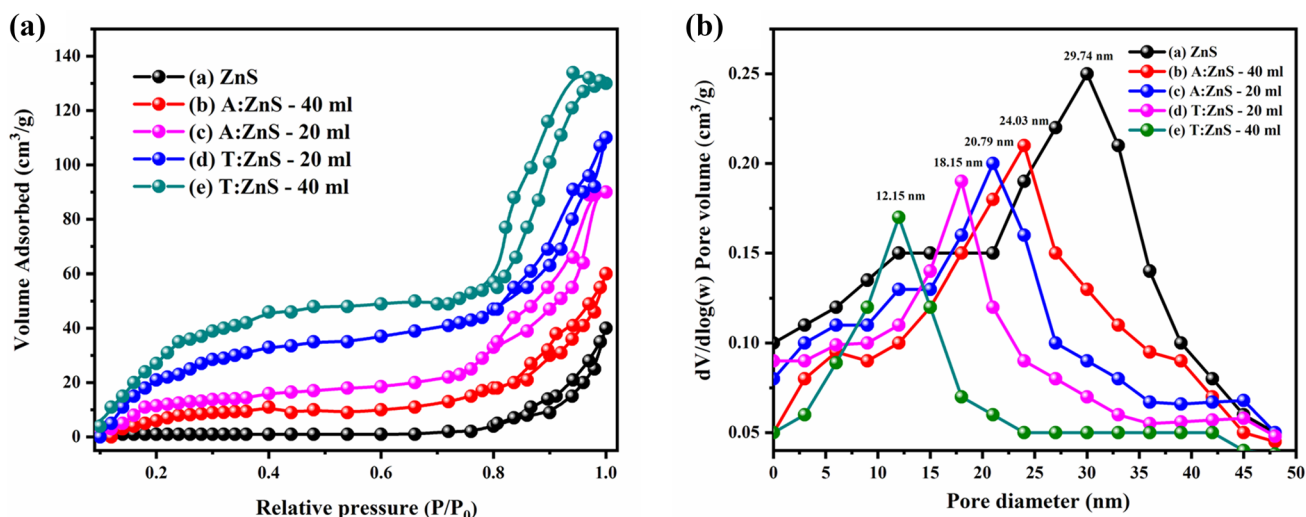


Fig. 10 BET surface analysis of ZnS/A:ZnS/T:ZnS nanoparticles. **a** Nitrogen adsorption–desorption isotherms curve. **b** Pore size distribution curve

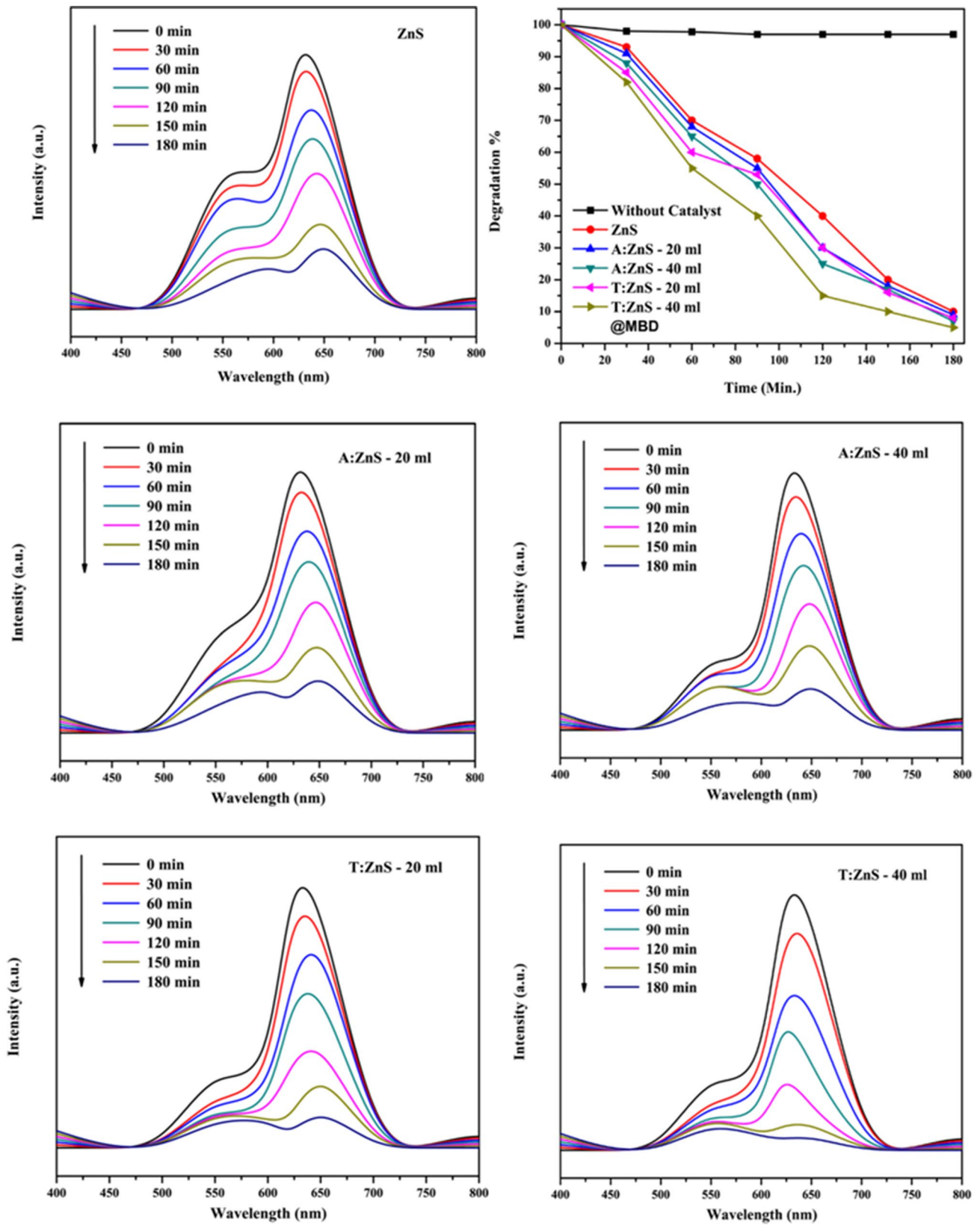


Fig. 11 UV–Visible spectra for photocatalytic degradation of methylene blue dye using ZnS/A:ZnS/T:ZnS nanoparticles

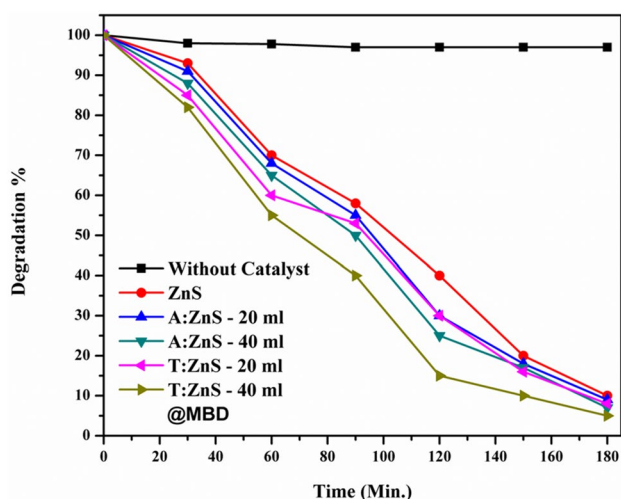


Fig. 12 Methylene blue dye degradation efficiency of ZnS/A:ZnS/T:ZnS nanoparticles

of ZnS, A:ZnS-20 ml, A:ZnS-40 ml, T:ZnS-20 ml, and T:ZnS-40 ml nanoparticles were observed to be 93%, 94%, 95%, 95%, and 98% after 180 min of irradiation time, respectively (see Fig. 12). It was observed that the T:ZnS-40 ml have maximum degradation efficiency than other nanoparticles. It was also observed that plant extract-capped ZnS nanoparticles have higher degradation efficiency than pure ZnS nanoparticles due to the presence of secondary metabolites which may be attributed to the reduction in electron–hole recombination [34]. Hence when the concentration of plant extract is increased, the degradation efficiency also increases. Here, we assume that plant extract may influence ZnS crystal growth with high surface-to-volume ratio which highly generate electron–hole pair at the tail states of conduction band and valance band under visible light irradiation. From this investigation, methylene blue dye degradation efficiency depends on the irradiation time, quantity, and quality of the photocatalyst [35]. Kikuchi et al. evaluated the role of the ROS in the reaction process, by the addition of hydroxyl radical scavenger. It was observed that the bactericidal activity was reduced by the addition of the scavenger, but the activity did not cease. The authors proposed that the presence of the more reactive hydrogen peroxide as the reason of continued bactericidal activity. Hence the anti-bacterial activity is a cooperative effect of all the ROS intermediates formed in the reaction process [36].

Further, the kinetic rate in the degradation of MB dye solution using ZnS/A:ZnS/T:ZnS catalyst was investigated according to the following pseudo-first order kinetics model. Fig. 13 depicts the plot of $\ln(C_t/C_0)$ versus Irradiation time for ZnS/A:ZnS/T:ZnS catalyst. This linear relationship of the plot indicates that degradation of MB dye

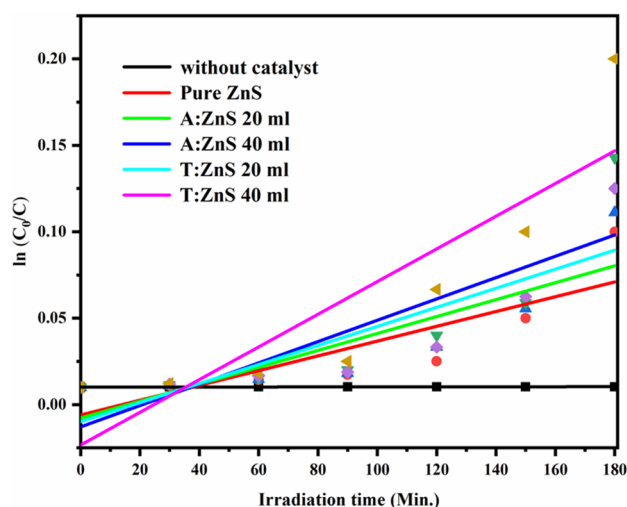


Fig. 13 Kinetic studies for the degradation of Methylene blue dye using ZnS/A:ZnS/T:ZnS nanoparticles

using ZnS/A:ZnS/T:ZnS catalyst obeys pseudo-first order kinetics and rate of expression is given by the following equations [37]

$$\ln(C_t/C_0) = kt \quad (7)$$

where k is constant of photodegradation rate (min^{-1}), C_0 is concentration of dye after self photocatalysis (mg/l), C_t is irradiation time. The kinetic rate constant of MB dye for ZnS, A:ZnS-20 ml, A:ZnS-40 ml, T:ZnS-20 ml, and T:ZnS-40 ml catalyst was estimated to be 0.071, 0.080, 0.091, 0.097, and 0.147 min^{-1} , respectively. These results suggest that T:ZnS-40 ml catalyst is 2 times better than pure ZnS catalyst.

Hence the stability and recyclability of the catalyst is crucial for dye degradation applications; herein, the stability and recycling test were carried out for MB dyes using A:ZnS-40 ml and T:ZnS-40 ml sample as catalysts and the resultant graph is shown in Fig. 14. After 6 consecutive cycle experiments, the T:ZnS-40 ml catalyst did not exhibit any major loss to activity, the catalysts lost only 1.85% of removal efficiency from their initial degradation efficiency. These results clearly indicated that the prepared T:ZnS-40 ml show evidence of high stability than A:ZnS-40 ml sample and it can be useful for potential application for environmental remediation under visible light.

4 Conclusion

In summary, the ZnS nanoparticles were successfully synthesized using different concentration of *Acalypha indica* (A:ZnS) and *Tridax procumbens* (T:ZnS) plant extracts.

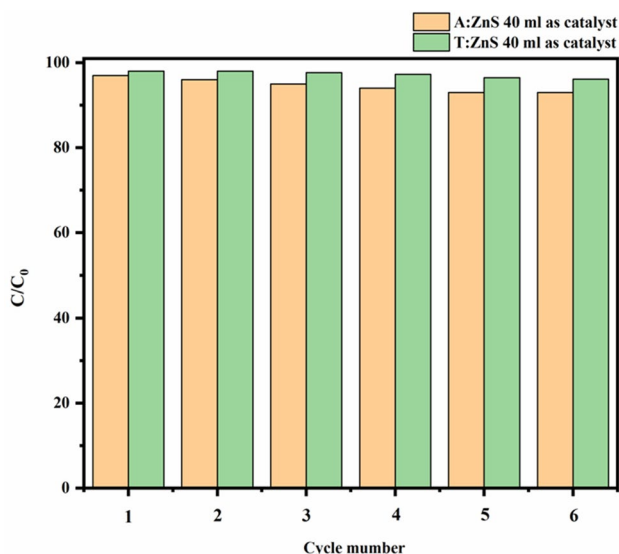


Fig. 14 Recycling test for the degradation Methylene blue dye using ZnS/A:ZnS/T:ZnS nanoparticles

XRD study revealed the formation of hexagonal phase of ZnS and average particle size was found to be 5–20 nm in diameter and this estimated grain size values are in agreement with the values obtained from the XRD and TEM images. The optical properties indicated that absorption edge shifted towards the higher (red shift) wavelength and band gap values of A:ZnS/T:ZnS nanoparticles prepared by using different plant extract concentration were found to decrease when compared with pure ZnS. FTIR spectra confirmed the presence of different biomolecules bonding from plant extracts which influence the growth of ZnS nanoparticles. The antibacterial activity of ZnS/A:ZnS/T:ZnS nanoparticles was investigated again with Gram-positive and Gram-negative bacteria and excellent inhibition zone was formed against *S. aureus* (Gram-negative) bacteria for T:ZnS-40 ml nanoparticles and plant extract-capped ZnS was found to give high inhibition zone when compared with pure ZnS. When the concentration of ZnS nanoparticles increased, inhibition zone also increased due to the presence of biomolecules and high surface area of ZnS crystal. Moreover, the effect of plant extract concentration positively influence on the structural, optical, and antibacterial behavior, and these results support the enhanced photocatalytic efficiency under visible light. The ZnS/A:ZnS/T:ZnS nanoparticles were found to have excellent photodegradation efficiency for methylene blue dye. From this investigation, 1.0 mg of T:ZnS-40 ml nanoparticles exhibited excellent methylene blue dye degradation efficiency (98%) under 180 min of the visible light irradiation which was two times better than pure ZnS. Hence, this novel green synthesis process might endow with considerable information to establish efficient photocatalysts and

innovative approach to eliminate natural refractory pollutants for waste water treatment.

Compliance with ethical standards

Conflict of interest The authors declare that they have no competing interests.

References

1. M. Sharma, S. Kumar, O.P. Pandey, J. Nanopart. Res. **12**, 2655–2666 (2010)
2. H. Labiadh, K. Lahbib, S. Hidouri, S. Touil, T.B. Chaabane, Asian Pac. J Trop. Med. **9**, 757–762 (2016)
3. M. Barberio, P. Barone, A. Oliva, Radiat. Phys. Chem. **81**, 642–646 (2012)
4. G.J. Lee, J.J. Wu, Recent development in ZnS photocatalysts from synthesis to photocatalytic applications. Powder Technol. **318**, 08–22 (2017)
5. U. Jabeen, S.M. Shah, S.U. Khan, Surf. Interfaces **6**, 40–49 (2017)
6. Z. Ye, L. Kong, F. Chen, Z. Chen, Y. Lin, Optik **164**, 345–354 (2018)
7. M. Sathishkumar, M. Saroja, M. Venkatachalam, Optik **182**, 774–785 (2019)
8. S. Ummartyotin, Y. Infahsaeng, Sust. Energy Rev. **55**, 17–24 (2016)
9. R. Subramanian, P. Subramaniyan, J.N. Ameen, V. Raj, Arab. J. Chem. **9**, 537–540 (2011)
10. M. Parthibavarman, S. Sathishumar, S. Prabhakaran, J. Mater. Sci: Mater. Electron. **29**, 2341–2350 (2018)
11. M. Parthibavarman, M. Karthik, P. Sathishumar, R. Poonguzhali, J. Iran. Chem. Soc. **15**, 1419–1430 (2018)
12. M. Parthibavarman, S. Sathishumar, S. Prabhakaran, M. Jayashree, R. Boopathi Raja, J. Iran. Chem. Soc. **15**, 2789–2801 (2018)
13. M. Sathishkumar, M. Saroja, M. Venkatachalam, Orient. J. Chem. **33**, 903–909 (2017)
14. K.R. Brain, T.D. Tuner, Bristol: Wright-Scientifica, 81–88 (1975)
15. S. Christudas, T.M. Kulathivel, P. Agastian, Asian Pac. J. Trop. Biomed., 159–161 (2012)
16. J. Chen, B. Hu, J. Zhi, Physica E **79**, 103–106 (2016)
17. S.K. Mani, S. Manickam, V. Muthusamy, R. Thangaraj, J. Nanostruct. **8**, 107–118 (2018)
18. A.W. Bauer, W.M. Kirby, J.C. Sherris, M. Turck, Am. J. Clin. Pathol. **45**, 493–496 (1966)
19. A.A. Mansur, H.S. Mansur, F.P. Ramanery, L.C. Oliveira, P.P. Souza, Appl. Catal. B Environ. **158**, 269–279 (2014)
20. Z. Ye, L. Kong, F. Chen, Z. Chen, Y. Lin, C. Liu, Optik **164**, 345–354 (2018)
21. U.S. Senapati, D. Sarkar, Indian J. Phys. **88**, 557–562 (2014)
22. L. Yue, S. Qi, J. Wang, J. Cai, B. Xin, Mater. Sci. Semicond. Process. **56**, 115–118 (2016)
23. C.H. Dipak, A. Kalita, S. Bardaloi, M.P. Kalita, J. Lumin. **210**, 269–275 (2019)
24. D. Ayodhya, G. Veerabhadram, J. Fluoresc. **26**, 2165–2175 (2016)
25. W. Zhang, X. Zeng, H. Liu, J. Lu, J. Lumin. **134**, 498–503 (2013)
26. M. Hudlikar, S.S. Joglekar, M. Dhaygude, K.M. Kodam, J. Nanopart. Res. **14**, 865–871 (2012)
27. P.S. Khiewa, S. Radimana, N.M. Huanga, S.M.D. Ahmed, K. Nadarajah, Mater. Lett. **59**, 989–993 (2005)

28. P. Iranmanesh, S. Saeednia, M. Nourzpoor, *Chin. Phys. B.* **24**, 046104 (2015)
29. S. Ham, D.J. Jang, *J. Environ. Chem. Eng.* **6**, 228–235 (2018)
30. C. Malarkodi, G. Annadurai, *Appl. Nanosci.* **3**, 389–395 (2013)
31. D. Liu, X. Li, Z. Shi, B. Zhu, X. Che, J. Yang, *J. Mater. Sci: Mater. Electron.* **29**, 11605–11612 (2018)
32. Y. Ding, L. Sun, Y. Jiang, S. Liu, M. Chen, M. Chen, Y. Ding, Q. Liu, *Mater. Sci. Eng. C* **67**, 188–194 (2016)
33. C. Lu, C. Liu, R. Chen, X. Fang, K. Xu, D. Meng, *J. Mater. Sci: Mater. Electron.* **27**, 6947–6954 (2016)
34. N. Kumbhojkar, V.V. Nikesh, A. Kshirsagar, S. Mahamuni, *J. Appl. Phys.* **88**, 6260–6265 (1999)
35. M. Sathishkumar, A.T. Rajamanickam, M. Saroja, *J. Mater. Sci: Mater. Electron.* **29**, 14200–14209 (2018)
36. Y. Kikuchi, K. Sunada, T. Iyoda, K. Hashimoto, A. Fujishima, *J. Photochem. Photobiol. A: Chem.* **106**, 51–56 (1997)
37. R.K. Chandrakar, R.N. Baghel, V.K. Chandra, B.P. Chandra, *Superlattices Microstruct.* **84**, 132–143 (2015)

Publisher's Note Springer Nature remains neutral with regard to jurisdictional claims in published maps and institutional affiliations.